JOURNAL OF GEOPHYSICAL RESEARCH, VOL. 112, C12007, doi:10.1029/2006JC003984, 2007

Spatial interpolation and filtering of surface current data based on open-boundary modal analysis

David M. Kaplan[1,2] and Francois Lekien[3,4]

Received 23 October 2006; revised 18 July 2007; accepted 5 September 2007; published 14 December 2007.

[1] The use of high-frequency (HF) radar surface current measurements are limited by spatial coverage gaps and sparse sampling. The normal mode (NMA) and open-boundary mode (OMA) current decomposition techniques developed by Lipphardt et al. (2000) and Lekien et al. (2004), respectively, produce smooth two-dimensional current fields by fitting data to a set of spatial modes. These methods have the advantages of incorporating the coastal boundary condition and providing a controllable level of spatial smoothing. While computation of and fitting to modes has been previously examined, variations and limitations of the technique have not been fully explored. Here we expand on the original OMA algorithm to incorporate radial currents produced by individual HF radars. Assimilating radial measurements maximizes use of available data and avoids the additional step and error of creating vector currents from radial data. We also develop techniques for dealing with spatially nonuniform data distributions and data gaps. Estimates of measurement error are propagated to evaluate the uncertainty of interpolated current fields. We illustrate our findings and assess the robustness of the OMA technique for calculating currents, divergences, and vorticities using HF radar data from Bodega Bay and Monterey Bay, California. Though care must be taken when using the technique as occasional shortage of data (e.g., temporary failure of a radar station) can produce erroneous fitted currents, OMA provides a robust mechanism for interpolating and filtering two-dimensional velocity measurements. Furthermore, OMA-derived errors provide a transparent and useful estimate of spatial patterns of uncertainty.

Citation: Kaplan, D. M., and F. Lekien (2007), Spatial interpolation and filtering of surface current data based on open-boundary modal analysis, *J. Geophys. Res.*, *112*, C12007, doi:10.1029/2006JC003984.

1. Introduction

[2] Recently, there has been a rapid expansion of the use of current measuring instruments, such as acoustic Doppler current profilers (ADCP) and high-frequency (HF) radars, for studying coastal circulation patterns. While these instruments describe coastal flow patterns, such as upwelling jets and wind-relaxation current reversals, with unprecedented detail [e.g., *Paduan and Rosenfeld*, 1996; *Kaplan et al.*, 2005], the data they produce are often too sparse for applications such as the computation of Lagrangian trajectories [*Kaplan and Largier*, 2006] and the identification of flow separatrices and coherent structures [*Lekien et al.*, 2005]. When trajectories are computed, the spatial gaps limit the area where particles can be tracked. Lagrangian trajectories and coherent structures are important for identifying fronts and understanding transport and mixing processes, such as plankton transport [*Bjorkstedt and Roughgarden*, 1997; *Kaplan and Largier*, 2006], oil spill evolution [*Hodgins*, 1994], pollution dispersal [*Lekien et al.*, 2005; *Coulliette et al.*, 2007], drifter coverage and deployment [*Olascoaga et al.*, 2006; *Shadden et al.*, 2007], and search and rescue missions [*Ullman et al.*, 2006]. Furthermore, instrument noise and sparse data limit the use of surface currents data for studying surface divergence and vorticity patterns. These patterns are, nevertheless, useful to understanding mesoscale patterns of coastal upwelling [*Kaplan and Largier*, 2006]. To overcome the limitations of these data sets, there is a clear need for efficient and effective techniques for interpolating and filtering two-dimensional current data.

[3] The open-boundary modal analysis (OMA) investigated in this paper interpolates and spatially filters two-dimensional current data, as well as provides an efficient means of calculating surface divergence and vorticity patterns [*Lipphardt et al.*, 2000; *Lekien et al.*, 2004]. The method is based on a set of linearly independent

[1]Institute of Marine Sciences, Earth and Marine Sciences, University of California, Santa Cruz, California, USA.
[2]Now at Centre de Recherche Halieutique, Institut de Recherche pour le Developpement, Sete, France.
[3]Mechanical and Aerospace Engineering, Princeton University, Princeton, New Jersey, USA.
[4]Now at École Polytechnique, Université Libre de Bruxelles, Brussels, Belgium.

0148-0227/07/2006JC003984$09.00

current modes that describe all possible current patterns inside a two-dimensional domain. The amplitude of those modes are then fit to current measurements inside the domain. As the modes depend only on the shape of the domain and can be calculated before they are fit to the data [*Lekien et al.*, 2004], the technique is well-suited for real-time data analysis and visualization. Fitted current fields are smooth throughout the domain and suitable for Lagrangian applications. As the technique is purely two-dimensional, it does not require a priori knowledge of the full three-dimensional circulation pattern and accurately estimates the surface circulation without necessitating additional assumptions (other than the coastal boundary condition). The effect of the vertical motion is, however, not filtered and can be observed in the surface divergence field.

[4] In this paper, we develop a practical guide for the application of OMA to two-dimensional velocity fields and we examine many details of the technique that have not been previously addressed. We improve the robustness of OMA by incorporating surface currents data as efficiently as possible, by comparing different parameterizations of the technique and by assessing uncertainties in fitted current fields. We also identify the limitations of the technique and suggest directions for future research.

[5] The paper is divided into three principal sections. The first section recaps the theoretical foundations of OMA, as well as discusses mode normalization and the calculation of surface divergence and vorticity. In the second section, we examine the fitting of mode amplitudes to current measurements. The fitting method is extended to assimilate directly radial current measurements generated by HF radars. We then develop techniques for dealing with nonuniform spatial distributions of data and use standard error propagation to calculate the uncertainty in fitted current fields. In the final section, we assess the robustness of the technique by applying it to current data from the Bodega Bay and Monterey Bay regions of north-central California.

2. Open-Boundary Modal Analysis

[6] We begin with a brief summary of the development of open-boundary modal analysis (see *Lekien et al.* [2004] for more details). Modal analysis of two-dimensional current data is based on the Hodge Decomposition [*Eiseman and Stone*, 1973] of an arbitrary two-dimensional field $\vec{u}$ into vorticity-free ($\vec{u}_\varphi$) and divergence-free ($\vec{u}_\psi$)components,

$$\vec{u} = \vec{u}_\varphi + \vec{u}_\psi \ , \tag{1}$$

each of which can be expressed in terms of scalar potentials,

$$\begin{array}{c} \vec{u}_\varphi = \nabla\varphi \\ \vec{u}_\psi = \hat{k} \times \nabla\psi, \end{array} \tag{2}$$

where $\vec{k}$ is a unit vector orthogonal to the horizontal plane. This decomposition leads to a pair of partial differential equations for the scalar potentials,

$$\begin{array}{c} \nabla \cdot \vec{u} = \Delta\varphi \\ \hat{k} \cdot \nabla\times \ \vec{u} = \Delta\psi, \end{array} \tag{3}$$

where $\nabla \cdot \vec{u}$ and $\hat{k} \cdot \nabla\times \ \vec{u}$ are the two-dimensional divergence and vorticity, respectively, of the current field, and $\Delta = \nabla^2 = \frac{\partial^2}{\partial x^2} + \frac{\partial^2}{\partial y^2}$.

[7] Though this decomposition of the current field can always be made, it is only unique once a set of boundary conditions for φ and ψ have been chosen. *Lipphardt et al.* [2000] and *Lekien et al.* [2004] chose to specify the normal component of flow along the boundary solely in terms of φ and to fix ψ along the boundary

$$\begin{array}{c} \hat{n} \cdot \vec{u}|_{\partial\Omega} = (\hat{n} \cdot \nabla\varphi)|_{\partial\Omega} \\ 0 = \psi|_{\partial\Omega}. \end{array} \tag{4}$$

This is a natural choice as the normal component of flow vanishes along any section of $\partial\Omega$ that is adjacent to land (i.e., it satisfies the free-slip boundary condition) and fixing ψ along the boundary simplifies solving its partial differential equation. Other choices for the boundary conditions are possible [*Lynch*, 1989], but, in general, they do not naturally incorporate the coastal boundary condition.

[8] Assuming the set of boundary conditions given in equation (4), the PDE in equation (3) can be solved by expanding φ and ψ into sets of interior eigenmodes, which have zero flow across the domain boundary, and a set of boundary modes, which account for inflow and outflow from the boundary. Using these modes, any arbitrary current field on the domain can be written as a linear combination of the modes [*Lekien et al.*, 2004].

[9] The interior eigenmodes for φ and ψ are defined by

$$\begin{cases} \Delta\varphi_i = \lambda_i^\varphi \varphi_i \\ (\hat{n} \cdot \nabla\varphi_i)|_{\partial\Omega} = 0 \end{cases} \quad \begin{cases} \Delta\psi_i = \lambda_i^\psi \psi_i \\ \psi_i|_{\partial\Omega} = 0. \end{cases} \tag{5}$$

Lekien et al. [2004] showed that the eigenvalues of these modes are necessarily negative and that the magnitudes of the eigenvalues are related to the fundamental spatial scales of the modes. Note that interior eigenmodes reduce to a two-dimensional Fourier transform if the domain is rectangular.

[10] The boundary modes are defined by

$$\begin{cases} (\Delta\varphi^b)|_\Omega = \dfrac{\oint_{\partial\Omega} g(s)ds}{\iint_\Omega dA} \equiv \dfrac{1}{A}\oint_{\partial\Omega} g(s)ds \\ (\hat{n} \cdot \nabla\varphi^b)|_{\partial\Omega} = \hat{n} \cdot \vec{u}^b|_{\partial\Omega} = g(s) \quad , \\ \iint_\Omega \varphi^b dA = 0 \end{cases} \tag{6}$$

where A is the total area of the domain, $\vec{u}^b = \nabla\varphi^b$ is the current field associated with the mode φ^b, and $g(s)$ is a function of the distance, s, along the boundary of the domain. The three conditions in equation (6) uniquely define φ^b in terms of $g(s)$ [*Lekien et al.*, 2004]. Note that the Laplacian of φ^b (i.e., the divergence of the boundary mode currents) is constant over the domain, and $g(s)$ vanishes along any section of the boundary that is closed (e.g., land).

[11] In the work by *Lipphardt et al.* [2000], the contribution of inflow and outflow is approximated from available current data or from a larger scale model by $g(s) = (\hat{n} \cdot \vec{u}|_{\partial\Omega})$, where $\vec{u}$ are the currents along the open boundary. When fitting current data to the modal expansion, the boundary mode is subtracted from the current data and the remainder, which satisfies the homogeneous boundary conditions, is fit to the interior eigenmodes.

[12] An alternative approach developed by *Lekien et al.* [2004], which we follow here, is to generate an infinite set of boundary modes, φ_i^b, based on any suitable complete basis, $\{g_i(s)\}$, of scalar L^2 functions defined on $\partial\Omega$. This set of boundary modes is then fit, along with the interior modes, to the data collected at the observing stations.

[13] A natural choice for the boundary functions, $\{g_i(s)\}$, is a discrete Fourier basis defined on the open boundary (and vanishing elsewhere)

$$\{g_i(s)\} = \left\{1, \ldots, \cos\left(2\pi i \frac{s}{l}\right), \sin\left(2\pi i \frac{s}{l}\right), \ldots\right\}, \tag{7}$$

where i is an integer, s is the arc length, measured counterclockwise from the start of the open boundary, and l is the total length of the open boundary. This basis set has the advantage that the divergence induced by the boundary mode vanishes (i.e., $\Delta\varphi_i^b = 0$) for all boundary modes except the one corresponding to $g_0(s) = 1$. Bases for domains with multiple disconnected open boundaries can be obtained as the union of basis sets for each individual piece of the open boundary [*Lekien et al.*, 2004].

[14] Any current field defined in a two-dimensional, bounded domain Ω can be expanded in terms of the interior and boundary modes,

$$\vec{u} = \sum_{i=1}^{\infty} \alpha_i^{\psi} \hat{k} \times \nabla\psi_i + \sum_{i=1}^{\infty} \alpha_i^{\varphi} \nabla\varphi_i + \sum_{i=0}^{\infty} \alpha_i^b \nabla\varphi_i^b. \tag{8}$$

This expansion is complete (i.e., valid for any bounded current field) and the mode coefficients are unique, provided that the boundary functions, $\{g_i(s)\}$, are all linearly independent of each other.

2.1. Mode Normalization

[15] There are two natural inner products on the space of current modes that can be used to normalize the modes. The first is based on the scalar functions themselves,

$$\langle \varphi, \varphi' \rangle = \frac{\iint_{\Omega} \varphi\varphi' dA}{\iint_{\Omega} dA} = \frac{1}{A} \iint_{\Omega} \varphi\varphi' dA \ . \tag{9}$$

The second is based on the currents derived from the scalar potentials,

$$\langle \vec{u}, \vec{u}' \rangle = \frac{1}{A} \iint_{\Omega} \vec{u} \cdot \vec{u}' dA. \tag{10}$$

The first of these inner products is appropriate for computing numerically the modes, but the second is more appropriate for fitting current data to the modes. If each mode is normalized so that

$$\|\vec{u}_i\|^2 \equiv \langle \vec{u}_i, \vec{u}_i \rangle = 1, \tag{11}$$

where $\vec{u}_i$ refers to the currents associated with any of the interior or boundary modes, then all modes will have the same average kinetic energy per unit area,

$$\frac{K_i}{A} \equiv \frac{1}{2} \langle \vec{u}_i, \vec{u}_i \rangle = \frac{1}{2} \tag{12}$$

Given this normalization, each coefficient, α_i, in equation (8) has the same units as the currents themselves and, therefore, can readily be compared both to the typical magnitude of the original current field and to the other coefficients. Therefore we will use the normalization in equation (10) throughout this manuscript.

[16] While the definition of the interior eigenmodes is unchanged by mode normalization (both sides of equation (5) are multiplied by the same number), the definition of the boundary modes is affected by the normalization. If we define $\tilde{\varphi}_i^b = \varphi_i^b / \|\vec{u}_i^b\|$, then the boundary functions scale according to

$$\tilde{g}_i(s) = g_i(s) / \|\vec{u}_i^b\| \ . \tag{13}$$

In practice, the boundary modes are calculated using a convenient set of boundary functions and the modes and the boundary functions are renormalized afterward using the equation above.

[17] It is readily observed that, given the definition of the inner product in equation (10), the interior modes are all mutually orthogonal. For example, the inner product of two divergence-free modes is

$$\begin{aligned} \langle \vec{u}_i | \vec{u}_j \rangle &= \frac{1}{A} \iint_{\Omega} \left(\hat{k} \times \nabla\psi_i\right) \cdot \left(\hat{k} \times \nabla\psi_j\right) dA \\ &= \frac{1}{A} \iint_{\Omega} \nabla\psi_i \cdot \nabla\psi_j dA \\ &= \frac{1}{A} \oint_{\partial\Omega} \psi_i \nabla\psi_j \cdot \hat{n} ds - \frac{1}{A} \iint_{\Omega} \psi_i \Delta\psi_j dA \\ &= -\frac{\lambda_j^{\psi}}{A} \langle \psi_i | \psi_j \rangle \quad = - \quad \frac{\lambda_i^{\psi}}{A} \langle \psi_i | \psi_j \rangle, \end{aligned} \tag{14}$$

because ψ_i vanishes on the boundary. The last equality above shows that the inner product $\langle \psi_i | \psi_j \rangle$ vanishes when $\lambda_i^{\psi} \neq \lambda_j^{\psi}$. When repeated eigenvalues exist (e.g., when the OMA domain is highly symmetric, such as a circle or square), a multidimensional eigenspace exists and the choice of the ψ_i for the multiple eigenvalue is not unique. It is, however, always possible to pick orthogonal modes ψ_i inside the eigenspace since the operator Δ is symmetric. As a result, one can always assume that $\langle \psi_i | \psi_j \rangle = \langle \vec{u}_i, \vec{u}_j \rangle = 0$ for any i, j. Similar computations reveal that the inner product between vorticity-free modes and the inner product between vorticity-free and divergence-free modes also vanish.

[18] On the other hand, the boundary modes are in general neither orthogonal to each other nor to the vorticity-free interior modes. For the product of two boundary modes, we have

$$\begin{aligned}\langle \vec{u}_i^b | \vec{u}_j^b \rangle &= \frac{1}{A}\iint_\Omega \nabla\varphi_i^b \cdot \nabla\varphi_j^b dA \\ &= \frac{1}{A}\oint_{\partial\Omega} \varphi_i^b \nabla\varphi_j^b \cdot \hat{n} ds - \frac{\Delta\varphi_j^b}{A}\iint \varphi_i^b dA \\ &= \frac{1}{A}\oint_{\partial\Omega} \varphi_i^b g_j(s) ds,\end{aligned} \tag{15}$$

which will not in general vanish. The product of an interior vorticity-free mode with a boundary mode is

$$\begin{aligned}\langle \vec{u}_i^b | \vec{u}_j^\varphi \rangle &= \frac{1}{A}\iint_\Omega \nabla\varphi_i^b \cdot \nabla\varphi_j dA \\ &= \frac{1}{A}\oint_{\partial\Omega} \varphi_i^b \nabla\varphi_j \cdot \hat{n} ds - \frac{1}{A}\iint \varphi_i^b \Delta\varphi_j dA \\ &= -\frac{1}{A}\iint_\Omega \varphi_i^b \Delta\varphi_j dA,\end{aligned} \tag{16}$$

which again will not in general vanish. The product of a divergence-free mode with a boundary mode does, however, vanish.

[19] The fact that the boundary modes and the vorticity-free interior modes are not orthogonal to each other has consequences for the interpretation of the mode coefficients in equation (8). Perhaps contrary to one's intuition, a mode coefficient is not necessarily the contribution of that mode to the overall kinetic energy, since there may be nonzero cross terms between modes. Equivalently, the projection of any mode onto the overall current field will not necessarily be the same as the coefficient of that mode in the expansion in equation (8). As the modes are not orthogonal, the orthogonal projections are not the best approximation of an arbitrary velocity field. This is an unavoidable consequence of the boundary conditions used to generate this modal current decomposition. One could, in principle, resolve this problem by creating a full set of modes that are mutually orthogonal using the Gram-Schmidt orthonormalization process, for example. This process is, however, not practical or desirable for many applications. First, the modes obtained loose their intrinsic length scale since the projection on each boundary mode (including the ones with very small length scales) has to be removed from each boundary mode. Furthermore, the orthonormalization of a boundary mode produces different results, depending on how many interior modes are selected.

[20] For these reasons, it is usually more efficient to allow nonorthogonal boundary modes and adapt the fitting method. If all the modes were orthogonal, the nowcast would be the orthogonal projection of the data onto these modes. That would lead to a highly efficient algorithm, where the component of each mode could be computed independently of the others. Owing to the nonorthogonality of the boundary modes, the coefficients of the modes must be determined all at once as described in section 3.

2.2. Divergence and Vorticity

[21] Once the current field has been expressed as a linear combination of the modes (equation (8)), its divergence and vorticity can be easily computed,

$$\begin{aligned}\nabla \cdot \vec{u} &= \sum_{i=1}^{\infty} \alpha_i^\varphi \lambda_i^\varphi \varphi_i + \sum_{i=0}^{\infty} \frac{\alpha_i^b}{A}\oint_{\partial\Omega} g_i(s) ds \\ \hat{k} \cdot \nabla \times \vec{u} &= \sum_{i=1}^{\infty} \alpha_i^\psi \lambda_i^\psi \psi_i.\end{aligned} \tag{17}$$

If $\partial\Omega$ possesses a single open boundary segment and a discrete Fourier basis has been chosen for the open boundary functions, the expression for the divergence reduces to

$$\nabla \cdot \vec{u} = \sum_{i=1}^{\infty} \alpha_i^\varphi \lambda_i^\varphi \varphi_i + \alpha_0^b g_0 \frac{l}{A}, \tag{18}$$

where l is the length of the open boundary segment and g_0 is the (constant) value of the boundary mode function (which may not be one after mode normalization). Notice that the vorticity and divergence inherit the smoothness properties and the characteristic length scales of the basis functions φ_i, ψ_i and φ_i^b. As a result, the equation above provides a smoothed, filtered and interpolated approximation of the vorticity and the divergence.

[22] It is, however, readily observed from equation (17) that the modal expansion of the currents always has zero vorticity at the domain boundary due to the definition of the interior divergence-free modes (equation (5)). The divergence field does not have this restriction because the φ_i do not necessarily vanish at the boundary.

[23] As vorticity will not, in general, vanish at the domain boundary for an arbitrary current field, this would appear to be in contradiction to the statement that the expansion in equation (8) is complete. In fact, the statement of completeness holds everywhere but the domain boundary (or, more mathematically, everywhere but a set of measure zero). While the Hodge Decomposition of the currents (equation (3)) yields a vorticity term that is nonzero at the boundary, the choice of homogeneous eigenmodes that vanish at the boundary to describe the vorticity necessarily produces an expansion that vanishes at the boundary. Nonetheless, the expansion is complete everywhere but the domain boundary in the limit of an infinite number of modes.

[24] This apparent contradiction is analogous to the expansion of a nonperiodic function on a one-dimensional finite segment using purely periodic functions (e.g., a Fourier expansion). In this case, for any finite number of basis functions, the expansion will approximately agree with the original function over most of the segment, except for a small region at the edges where the expansion will vary rapidly so that the full expansion is periodic. The extent of the area of disagreement between the expansion and the original function decreases as the number of basis functions increases (provided that the modes are ordered by decreasing length scales). This is a direct consequence of the fact that the disagreement can only occur, in the limit of an infinite number of modes, at the end points of the

segment. Similarly, for the expansion of a two-dimensional current field, such as the coastal currents in this paper, the vorticity field disagrees with that of the original current field near the domain boundary over a spatial scale approximately given by the scale of the highest-order mode used in the expansion (Figure 1). Furthermore, the modal fit can also introduce spatial variability into a spatially homogeneous vorticity pattern (Figure 2), analogous to the effects of a Fourier decomposition with a finite number of basis functions.

3. Fitting Data to the Modal Expansion

[25] Available current measurements are typically fit to a set of modes describing possible current patterns in a finite domain via a least squares minimization problem [*Lipphardt et al.*, 2000; *Lekien et al.*, 2004]. The cost function to minimize is given by

$$\zeta = \sqrt{\sum_{m=1}^{M}\left[W_m^u\left(\sum_{n=1}^{N}(\alpha_n u_n(\vec{x}_m)) - u_m^{mes}\right)^2 + W_m^v\left(\sum_{n=1}^{N}(\alpha_n v_n(\vec{x}_m)) - v_m^{mes}\right)^2\right]}. \tag{19}$$

Here $\vec{u}_m^{mes} = (u_m^{mes}, v_m^{mes})$ are a set of M current measurements at positions $\vec{x}_m$ inside the domain. $\vec{u}_n(\vec{x}_m) = (u_n(\vec{x}_m), v_n(\vec{x}_m))$ are the current fields associated with the N modes to which the data is to be fit evaluated at the location of the current measurements. In this section, we do not discriminate between divergence-free, vorticity-free and boundary modes (i.e., the index n runs over all mode types). The weighting factors, W_m^u and W_m^v, can be used to account for known measurement error or correlations among measurements [*Lipphardt et al.*, 2000; *Chu et al.*, 2003]. In the absence of information about the measurement error and error covariance, the weights can be set to one (i.e., equal weights).

[26] Minimization of the error function defined in equation (19) with respect to the α_n gives

$$\sum_{m=1}^{M}\left[W_m^u\left(\sum_{n=1}^{N}(\alpha_n u_n(\vec{x}_m)) - u_m^{mes}\right)u_j(\vec{x}_m) + W_m^v\left(\sum_{n=1}^{N}(\alpha_n v_n(\vec{x}_m)) - v_m^{mes}\right)v_j(\vec{x}_m)\right] = 0 \quad \forall\ j. \tag{20}$$

This set of linear equations can be solved for the α_n using standard linear algebra packages, provided that the number of current measurements exceeds the number of modes (i.e., the system is overdetermined).

[27] In practice, N, the number of modes used is finite and the nowcast can only describe spatial variability up to a specified minimum spatial scale, which corresponds to the mode with the smallest features (e.g., eddy diameter). When using Fourier basis functions, it is natural to associate the spatial scale of boundary modes with half the wavelength of the boundary function (i.e., the first nontrivial boundary mode will have a length scale equal to half the length of the open boundary). The spatial scale of interior modes was determined by *Lekien et al.* [2004] on the basis of the length scale of the entire domain and the square root of the ratio between the smallest eigenvalue of all (divergence-free or vorticity-free) interior modes and the eigenvalue of the mode of interest,

$$d_i = D\sqrt{\frac{\lambda_1}{\lambda_n}}, \tag{21}$$

where d_i is the length scale of the mode, D is the characteristic length scale of the domain (e.g., the diameter or smallest side of the domain), λ_1 is the smallest eigenvalue (typically from a vorticity-free mode) and λ_i is the eigenvalue of the mode of interest.

[28] Another approach to determining the length scale of interior modes is to associate the length scale of a mode on an arbitrary domain with the length scale of a mode with the same eigenvalue on a square domain of the same area (B. Lipphardt, personal communication, 2006). The length scale of the mode on the square domain is taken as half the wavelength of the mode

$$d_i = \frac{\pi}{\sqrt{\lambda_i}}. \tag{22}$$

This approach assumes that the arbitrary domain is roughly a square and produces similar results to equation (21) for domains whose aspect ratio is not far from one.

[29] Regardless of the specific formula used to define the length scale of the modes, this length scale decreases when the eigenvalue of the mode increases. As a result, selecting the number of modes that will be used in a nowcast can be done by selecting a threshold on the smallest length scale that will be resolved in the nowcast. This length scale must of course be greater than the minimum length scale of the data itself (i.e., greater than roughly 3 km for most 12 MHz HF radars).

3.1. Using Radial Measurements

[30] The fitting process described above is based on minimizing the mismatch between the nowcast and the total vector current measurements (i.e., both components of the velocity). However, a single HF radar instrument only measures the magnitude of the surface current along the direction from the radar to the location of the measurement. These data are typically referred to as radial currents or simply radials. Data from two or more instruments must be combined to resolve the total current velocity at a point. During the normal, non-OMA process of combining radial currents, a considerable percentage of the available data points cannot be used because, at a particular location, there might be information available from only one radar or the spread of angles among radials is insufficient to resolve the velocity vector (Figure 3b). These data can, however, be used to (partially) constrain the fit of current modes to the data. In fact, there is nothing particularly special about the choice of the u and v components in equation (19), and any

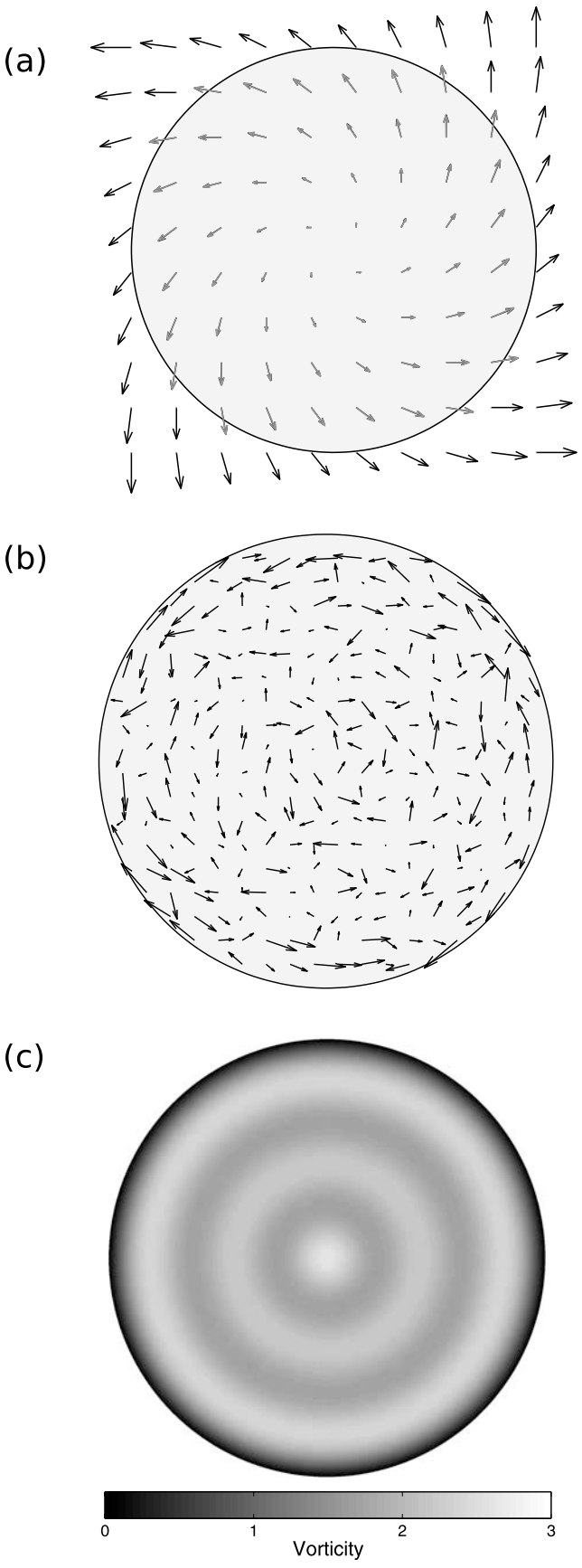

measurement of any component of the current velocity at a point can be used in the cost function.

[31] The appropriate generalization of the quadratic cost function is

$$\zeta = \sqrt{\sum_{m=1}^{M}\left[W_m^r\left(\sum_{n=1}^{N}(\alpha_n\vec{u}_n(\vec{x}_m))\cdot\hat{r}_m - u_m^r\right)^2\right]}, \qquad (23)$$

where $\hat{r}_m$ is a unit vector and u_m^r is a measurement of the component of the current at $\vec{x}_m$ along the direction of $\hat{r}_m$. This formula reduces to equation (19) when the $\hat{r}_m$ are along the x and y directions and can be used equally well with total vectors. Furthermore, equation (23) can be used to assimilate mixed data from a variety of different instruments types at once.

3.2. Spatially Inhomogeneous Data: Data Gaps

[32] Difficulties arise when using modal current decomposition to interpolate and spatially smooth surface current measurements in the presence of large spatial gaps in the original data. When current measurements with considerable spatial gaps are fit to a set of modes using equation (19) or equation (23), unphysically large fitted currents can occur in areas without data if the gaps are larger than the smallest spatial scale of the modes (Figure 4b). This occurs because the mode amplitudes are not sufficiently constrained by the data. The coefficients of one or more modes can become large without increasing the cost function so long as the resulting current field cancels everywhere outside the gaps. This phenomenon is particularly noticeable when data is lacking along open boundaries of the domain, since the boundary modes typically have small and nearly uniform current fields throughout the interior of the domain.

[33] The most conservative approach to this problem is to limit the number of modes used to those whose spatial scale is larger than the largest gap. In this case, the fit will always be sufficiently constrained. This solution is, however, not generally desirable since fewer modes can be used and substantial spatial smoothing can occur over the entire domain, even if the gaps are located in just one part of the domain. Furthermore, if fewer modes are used, then a smaller percentage of the overall spatial variance in the original current field will be represented in the fitted currents. This, in turn, introduces larger uncertainties

Figure 1. (a) Currents, (b) difference between original and fitted currents, and (c) vorticity from the OMA fit on a circular domain to a current field given by $\vec{u} = (u, v) = (x - y, x + y)$ using 85, 67, and 35 vorticity-free, divergence-free, and boundary modes, respectively. In Figure 1a, the original current field is shown in black, while the fitted vectors are in gray. In Figure 1b, the difference between original and fitted vectors is shown after being magnified 40 times. The true divergence and vorticity maps for this current field are constant over space with a value of 2 (not shown). The divergence map from the expansion (not shown) agrees with the true field, but the vorticity map (Figure 1c) differs due to the requirement of the expansion that vorticity vanish at the domain boundary.

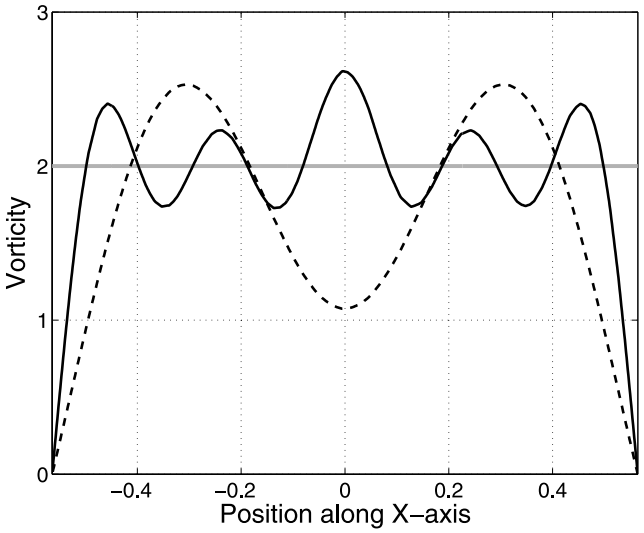

Figure 2. Vorticity along the x axis from the OMA expansion of a current field given by $\vec{u} = (u, v) = (x - y, x + y)$. The horizontal gray line is vorticity for the original current field. The dashed black curve is the vorticity from a fit involving 10 divergence-free modes (in addition to the other modes), while the solid black curve is from a fit using 67 divergence-free modes. Note that only a few of these modes contribute significantly to the vorticity map. For the dashed curve, two modes contribute to the vorticity, while for the solid curve, five divergence-free modes have coefficients significantly different from zero.

in integrative quantities of the current field, such as Lagrangian trajectories. These issues are particularly problematic if the gaps occur infrequently in time (e.g., because of occasional equipment failure).

[34] Another approach to resolving spatial gaps is to artificially constrain the fit so that it produces physically reasonable current fields even if there are gaps. These fields will not be based on current measurements in gap areas and, therefore, we should not expect that the modal fit will represent the currents accurately inside the gaps. This is, however, acceptable if gaps occur infrequently and one is mainly interested in temporal averages (e.g., subtidal flow fields) or integrative (e.g., Lagrangian trajectories) properties of the current field.

[35] This additional constraint on the fit is achieved by adding an extra term to equation (23) that prohibits the coefficient of any one mode from becoming too large. The introduction of such a "smoothing" (or regularizing) term in a cost function is common in optimization problems [see, e.g., *Amit*, 1994; *Pottmann and Leopoldseder*, 2003; *Brunnet et al.*, 1997]. There are many possibilities for the smoothing term. Nevertheless, if we wish to keep a linear least squares optimization problem, the most natural choice for the new metric is

$$\zeta = \sqrt{\sum_{m=1}^{M}\left[W_m^r\left(\sum_{n=1}^{N}(\alpha_n\vec{u}_n(\vec{x}_m))\cdot\hat{r}_m - u_m^r\right)^2\right] + \frac{M}{2}\sum_{n=1}^{N}\kappa_n\alpha_n^2}. \tag{24}$$

The second term in the equation above creates a penalty on large mode coefficients. We will refer to this term as the homogeneous smoothing term.

[36] Minimization of this function with respect to the α_n yields the final set of linear equations that can be solved for the mode coefficients,

$$\sum_{m=1}^{M}\left[W_m^r\left(\sum_{n=1}^{N}(\alpha_n\vec{u}_n(\vec{x}_m))\cdot\hat{r}_m - u_m^r\right)(\vec{u}_j(\vec{x}_m)\cdot\hat{r}_m)\right] + \frac{M}{2}\kappa_j\alpha_j = 0 \quad \forall \quad j. \tag{25}$$

[37] Notice that the effect of the additional term is to reinforce the diagonal of the linear system above. Standard results in numerical analysis can be used to determine the beneficial effect of the smoothing term on the stability of the solution. Sufficiently large coefficient κ_n guarantee a diagonally dominant matrix and, hence, bounded, physical solutions, no matter how singular the initial problem is.

[38] The goal of the additional term is to avoid large velocities, hence, it is natural to associate the values of the coefficients κ_n with the maximum velocity of the associated mode. Therefore a suitable choice for the κ_n is

$$\kappa_n = \kappa\|\vec{u}_n\|_\infty^2 , \tag{26}$$

where $\|\vec{u}_n\|_\infty$ is the maximum current magnitude of the nth mode in the domain. The average current velocity of the mode over the domain (which is one for normalized modes) can also be used, but the definition in equation (26) is appropriate as the goal is to avoid large current velocities. This choice leaves only one dimensionless parameter, κ, to determine. The value of κ can be chosen on the basis of the amount of control that one wishes to exercise over the coefficients. Application of the technique to current data from Bodega Bay and Monterey Bay indicates that values in the range of 10^{-4}–10^{-2} constrain unphysical current vectors without decreasing substantially the RMS difference between fitted and observed current measurements (section 4).

3.3. Spatially Inhomogeneous Data: Data Density

[39] The fit of current measurements to the modes can also be affected by data that is unevenly, but continuously, distributed in space. This problem is particularly severe when radial current data is directly fit to the modes, since there is generally a much higher density of radial measurements close to the radars. The true independence of the many radial measurements close to the radars has not been adequately established, and, therefore, there is the risk that the total current velocity is unjustly locally overdetermined by these measurements. In these cases, each individual measurement does not contribute as much information as other, more isolated data. When determining the mode coefficients, it is important to consider the data distribution, prioritize isolated independent measurements, and avoid distortion due to contradicting data in a very small, but highly sampled region.

[40] One approach to dealing with this problem is to use the weights, W_m^r, in equation (24) to adjust the contribution of each current measurement to the fit. For example, one can decrease the weight of a particular current measurement

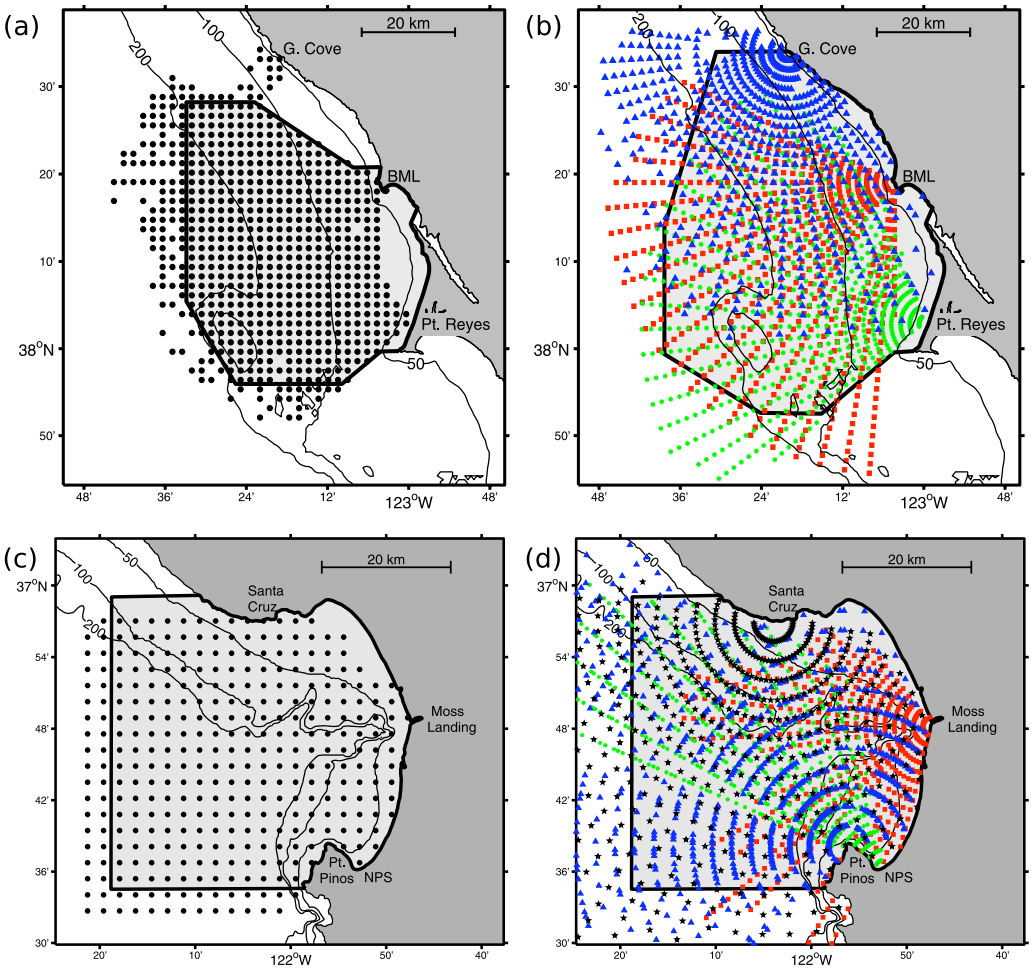

Figure 3. Average (a, c) total and (b, d) radial vector coverage by HF radars from Bodega Bay, California, and Monterey Bay, California. In Figures 3a, 3b, and 3c, markers indicate grid points that had coverage more than 70% of the time during the period of available data for each site. In Figure 3d, markers indicate radial grid points that had coverage more than 20% due to several changes in the location of the radial grid points over the time period. The gray areas with the solid black border are the (a) small Bodega, (b) large Bodega, and (c, d) Monterey domains over which modal current decomposition was performed. Note the lack of coverage by total current vectors to the north and east of the small Bodega domain boundary (Figure 3a), despite the existence of considerable radial current data in the area (Figure 3b).

to the fit when there is a high density of current measurements within a certain distance of the measurement location (i.e., the weight is inversely related to the data density for high densities). The appropriate distance within which to look for additional measurements is instrument (e.g., HF radar operating frequency) and location (e.g., spatial scale of current variability) dependent, but should correspond to the spatial scale over which one expects to be able to make an independent current measurement. For the 12 MHz HF radars used in this study, we chose a spatial scale of 2 km.

[41] More complicated schemes are also possible. For example, one could take into account the number of different instruments producing measurements in an area and the angle spread of the current measurements (e.g., through the geometric dilution of precision (GDOP) [*Chapman et al.*, 1997]), as well as any measure of the observation error. However, these more complicated schemes will not be further discussed or used in this manuscript.

3.4. Error Propagation

[42] While open-boundary modal analysis describes how to fit current data to a set of modes, it provides no estimate of the uncertainty associated with this fit. If velocity measurements come with an associated error estimate, then this information can be used to estimate the uncertainty associated with the mode coefficients using standard error propagation (e.g., following *Brandt* [1983]). We first make the following definitions to express the fit to the modes as a matrix equation:

$$\begin{aligned}
[\mathbf{D}]_m &= u^r_m, \\
[\boldsymbol{\alpha}]_n &= \boldsymbol{\alpha}_n, \\
[\mathbf{U_D}]_{mn} &= \vec{u}_n(\vec{x}_m)\cdot\hat{r}_m, \\
[\mathbf{W}]_{mk} &= \boldsymbol{\delta}_{mk} W^r_m, \\
[\boldsymbol{\kappa}]_{nj} &= \boldsymbol{\delta}_{nj}\frac{M}{2}\boldsymbol{\kappa}_n,
\end{aligned} \tag{27}$$

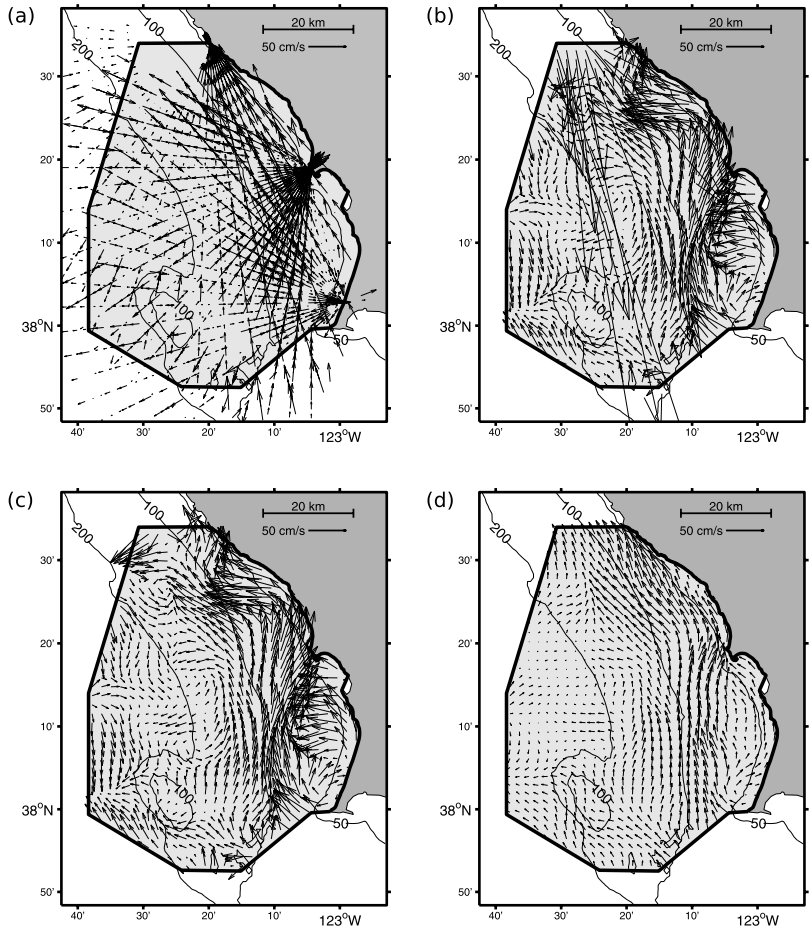

Figure 4. (a) Coverage by radial current vectors on 30 July 2003 1500 PST, and the fit to those radial vectors on the large domain for several values of the coefficient of the homogeneous smoothing term, κ, where κ is (b) 0, (c) 10^{-4}, and (d) 10^{-1}. Fits were performed using a minimum mode spatial scale of 5 km. Note the extremely large fitted current velocities in the upper left-hand corner of the domain where there is insufficient current data to constrain the fit when $\kappa = 0$ (Figure 4b).

where bold quantities on the left are column vectors or two-dimensional matrices (as determined by the number of indices), and brackets with indices to the lower right are used to indicate a particular element of these matrices. Here δ_{ij} is Kronecker's delta (i.e., $\delta_{ij} = 1$ if $i = j$ and 0 otherwise). With these definitions, equation (25) can be rewritten as

$$\mathbf{U_D}'\mathbf{W}\mathbf{D} = [\mathbf{U_D}'\mathbf{W}\mathbf{U_D} + \kappa]\boldsymbol{\alpha}. \tag{28}$$

where primes ($'$) indicate matrix transposes. Given a matrix, $\mathbf{C_D}$, of covariances among current measurements, the covariance matrix of $\boldsymbol{\alpha}$ is

$$\mathbf{C}_\alpha = \left[\mathbf{T}'(\mathbf{U_D}'\mathbf{W}\mathbf{C_D}\,\mathbf{W}'\mathbf{U_D})^{-1}\mathbf{T}\right]^{-1}, \tag{29}$$

where $\mathbf{T}$ is

$$\mathbf{T} = \mathbf{U_D}'\mathbf{W}\mathbf{U_D} + \kappa. \tag{30}$$

The matrix $\mathbf{C}_{\boldsymbol{\alpha}}$ gives the variances (diagonal elements) and covariances (off-diagonal elements) of the mode coefficients.

[43] Often, only a variance estimate for each velocity measurement or a single error estimate for all measurements is available, and there is no information regarding the covariability among data measurements. The lack of information about covariability between radial current measurements is an important weakness in our current understanding of the error structure of HF radar data. In the absence of covariability information, the simplest choice for $\mathbf{C_D}$ is to use a diagonal matrix with the variance estimates along the diagonal. Though this formulation overestimates the number of independent current measurements (and therefore underestimates the variances in C_α), it has been used in the past in the context of generating total currents from radial currents [*Lipa*, 2003]. A diagonal $\mathbf{C_D}$ is used for the results presented in section 4, but the developments below are applicable for an arbitrary covariance matrix.

[44] The covariance matrix for the mode coefficients, $\mathbf{C}_{\boldsymbol{\alpha}}$, can be used to provide an uncertainty estimate of the modal fitted current velocities. The modal fitted current velocity at a point, $\vec{x}$, is given by

$$\vec{u}_F(\vec{x}) = \mathbf{U}\boldsymbol{\alpha}, \tag{31}$$

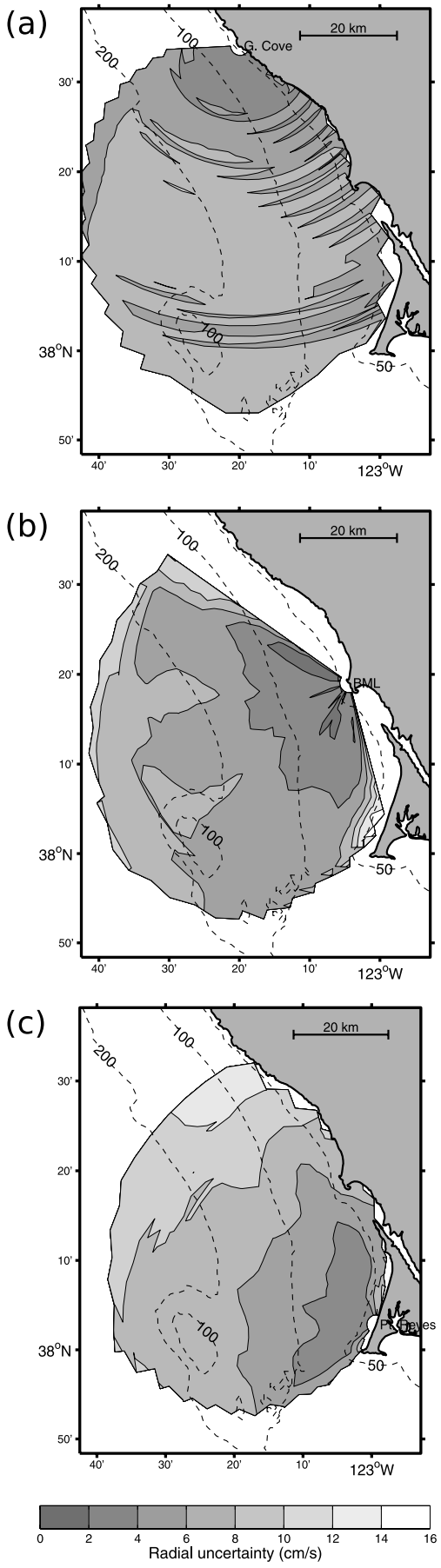

Figure 5. Average measured radial uncertainty for May–September 2003 from HF radars located at (a) Gerstle Cove, (b) Bodega Marine Laboratory, and (c) Point Reyes. Note that only radial grid points inside the large Bodega OMA domain were included in these uncertainty maps.

where

$$[\mathbf{U}]_{in} = u_{n,i}(\vec{x}) \tag{32}$$

and i is 1 or 2 (indicating the u or v component of the velocity, respectively). Therefore the covariance matrix of the fitted velocity is

$$\mathbf{C_F} = \mathbf{U}\mathbf{C}_\alpha\mathbf{U}'. \tag{33}$$

This expression can be suitably generalized to produce the covariance matrix for fitted velocities over the entire domain. The square root of the sum of the u and v variances has the units of current velocity, and is invariant under rotation of the coordinate system. It is one suitable measure of the overall uncertainty in an individual fitted current velocity.

3.5. Software Tools

[45] Several software packages have been developed to construct modes for modal current decomposition and to fit those modes to current measurements. Here is a partial list of those tools.

[46] 1. Randolph E. Bank's PLTMG is a package for solving elliptic partial differential equations and can be used to generate modes on an adaptive unstructured mesh. The Fortran code for PLTMG is available at http://www.scicomp.ucsd.edu/~reb/software.html.

[47] 2. A package written in C++ for computing interior and boundary modes using Rice University's sparse eigenvalue solver, ARPACK, and the University of Florida's sparse linear system solver, UMFPack, is available at http://www.lekien.com/~francois/software/oma.

[48] 3. A package written in C++ and using the GNU Scientific Library (GSL) for fitting HF radar data or other data sources to a set of modes is available at http://www.lekien.com/~francois/software/oma.

[49] 4. OpenMA is a Matlab toolbox that facilitates the use and automation of modal current decomposition. In addition to generating modes and producing interpolated current fields, the toolbox generates uncertainty maps and simple Lagrangian trajectories based on the fitted current field. OpenMA is available at https://erizo. pmc.ucsc.edu/COCMP-wiki/index.php/Documentation:OpenMA_Matlab_Toolbox and was used to generate the numerical results in this paper.

4. Application of OMA to Current Measurements

[50] We applied the modal current decomposition technique to hourly current data from two sites in California: Bodega Bay and Monterey Bay. The principal data set used here is from a three instrument array of HF radar stations near Bodega Bay (Figures 3a and 3b). Current measurements are from the spring and summer of 2003 and consist

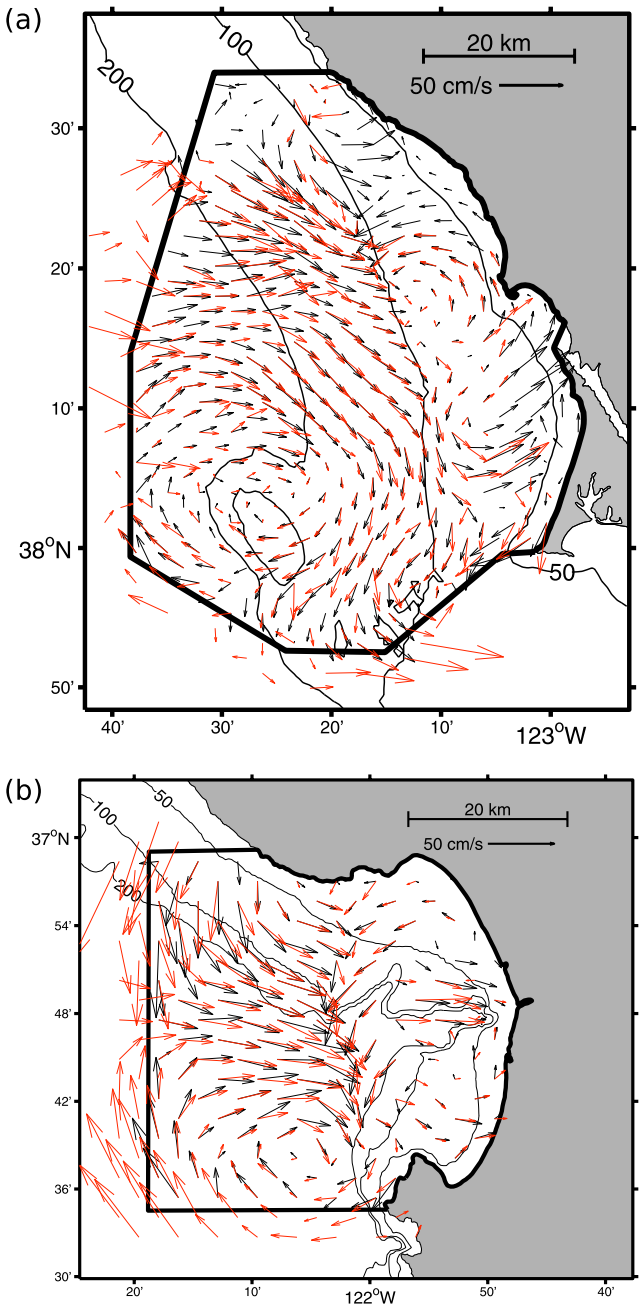

Figure 6. Modal-fitted current vectors (black) and current vectors calculated via the standard non-OMA method (red) for (a) 25 August 2003 0900 PST in Bodega Bay and (b) 13 August 2006 16:00 PST in Monterey Bay. In both cases, the minimum spatial scale of the modes is 5 km and the coefficient of the homogeneous smoothing term, κ, is 10^{-4}. The number of current vectors displayed has been reduced by half to improve visibility of the individual vectors.

of radial current measurements, as well as total current measurements derived from these radial measurements. For more details on the Bodega Bay HF radar array, as well as the analysis and processing of the data set, see *Kaplan et al.* [2005] and *Kaplan and Largier* [2006]. As an additional test of the OMA technique, we also applied the OMA technique to one week (8–15 August 2006) of radial current measurements from four HF radar instruments in Monterey Bay (Figures 3c and 3d [see also *Paduan and Rosenfeld*, 1996]). Basic processing and analysis of this data was similar to that of data from Bodega Bay.

[51] Modal current decomposition was applied to the data sets using several domains. Two Bodega domains were used, a large domain suitable for fits of radial current measurements and a small domain appropriate for fits of totals data or a reduced set of radial measurements (Figures 3a and 3b). These domains were chosen to be of maximum possible spatial extent with the goal of examining the sensitivity of OMA to the availability of data and the presence of data gaps. A single domain was used in Monterey Bay (Figure 3c). On each of these domains, all modes with a spatial scale greater than 5 km were calculated. This produced 241, 176 and 130 modes on the Bodega large, Bodega small and Monterey domains, respectively. Fits were performed using minimum spatial scales of 5 km (all modes) or 10 km (a subset of the modes calculated).

[52] Several different parameter values were used to test the sensitivity of the OMA technique. The value of κ (the homogeneous smoothing term in the fit; section 3.2) ranged from 0 to 10. Two error values were produced for each fit, one based on the assumption of a uniform uncertainty of 7.5 cm s^{-1} (approximately the mean measured radial current standard deviation) for all radial current measurements and the other based on the measured radial current variances (from repeated radial current measurements over the period of one hour; Figure 5). Fits were also bootstrapped (i.e., repeated after resampling the original data set) 40 times to produce an independent measure of the uncertainty in the fit. Finally, fits to radial current data were performed both with and without a nonuniform weighting of the measurements based on data density (see section 3.3). All data within 2 km of a point were used to calculate the density at that location.

[53] At times, temporal subsets of the data sets based on spatial coverage of data or alongshore wind stress were analyzed separately. In the analysis of Bodega Bay data, spatial coverage of total current measurements is defined as the number of good measurements inside the domain. Spatial coverage of radial currents (or lack thereof) is measured in terms of the total area inside the domain for which there are no radial current measurements within 2 km. These measures of spatial coverage are used to select out periods with good and bad data coverage for the Bodega Bay array. For the Monterey Bay data, the 42 hours of data for which only three HF radars were functioning were analyzed separately. These time periods generally had far lower coverage by radial and total current measurements than periods when all radars were functioning.

[54] Alongshore wind stress was used to divide the Bodega data set into periods of upwelling favorable winds and periods of relaxation of alongshore winds. Wind stress was derived from measurements made at the NDBC 46013 buoy (38.23 N 123.32 W; approximately 25 km west of Bodega Bay on the 123 m isobath). If the daily average alongshore wind stress was equatorward and greater in magnitude than 0.15 N m^{-2}, then the time period was defined as upwelling favorable, whereas if the wind stress magnitude was less than 0.05 N m^{-2}, it was considered a relaxation period. An extensive discussion of this division,

as well as a description of the wind stress data set used in this calculation, is given by *Kaplan and Largier* [2006].

4.1. Visual Comparison Between Modal-Fitted Currents and Total Current Measurements

[55] Modal fits using modes with a minimum spatial scale of 5 km to radial and total current measurements from Bodega Bay and Monterey Bay generally compared quite well to total current measurements (Figure 6). Over most of the domain, currents were aligned and of similar magnitudes. Typical RMS differences between fitted and total currents were of order 5–10 cm/s and average directional differences were less than 5 degrees (Figures 7 and 8). These RMS differences are considerable compared to the RMS velocity of the total currents themselves (typically 20–40 cm/s; given by RMS differences when κ is so large that fitted currents are small as shown on the right-hand side of Figures 7 and 8). Nevertheless, they are of the same order as the instrument uncertainty [*Kaplan et al.*, 2005] and are consistent with the higher level of smoothing in the fitted currents (5 km versus 2 km).

[56] There were considerable differences between the two in some areas, but these were generally associated with regions where confidence in the total current measurements was relatively low (e.g., far from the radars or along the line of sight between radars), where total current measurements are varying on spatial scales smaller than that of the modes, or close to the coast where fitted currents are constrained to have no flow through the closed boundary. Fits to modes with a minimum spatial scale of 10 km corresponded well to total current measurements (not shown), but not as well as those to modes with a 5 km spatial scale. This is not surprising as a smaller percentage of the overall spatial variability in the flow pattern is represented by a fit to fewer modes.

4.2. Effect of the Homogeneous Smoothing Term

[57] The homogeneous smoothing term was added to the fit to avoid large, unphysical currents in areas where data is not available (see section 3.2). In the absence of this term, fitted currents in data gaps larger than the smallest spatial scale of the modes are large and unpredictable (Figure 4b). With this term, currents in data gaps are considerably reduced (Figures 4c and 4d). For small values of κ, this additional term in the fit has little affect on the fitted currents in areas where data is plentiful (Figure 4c), but for larger values there is a substantial decrease in

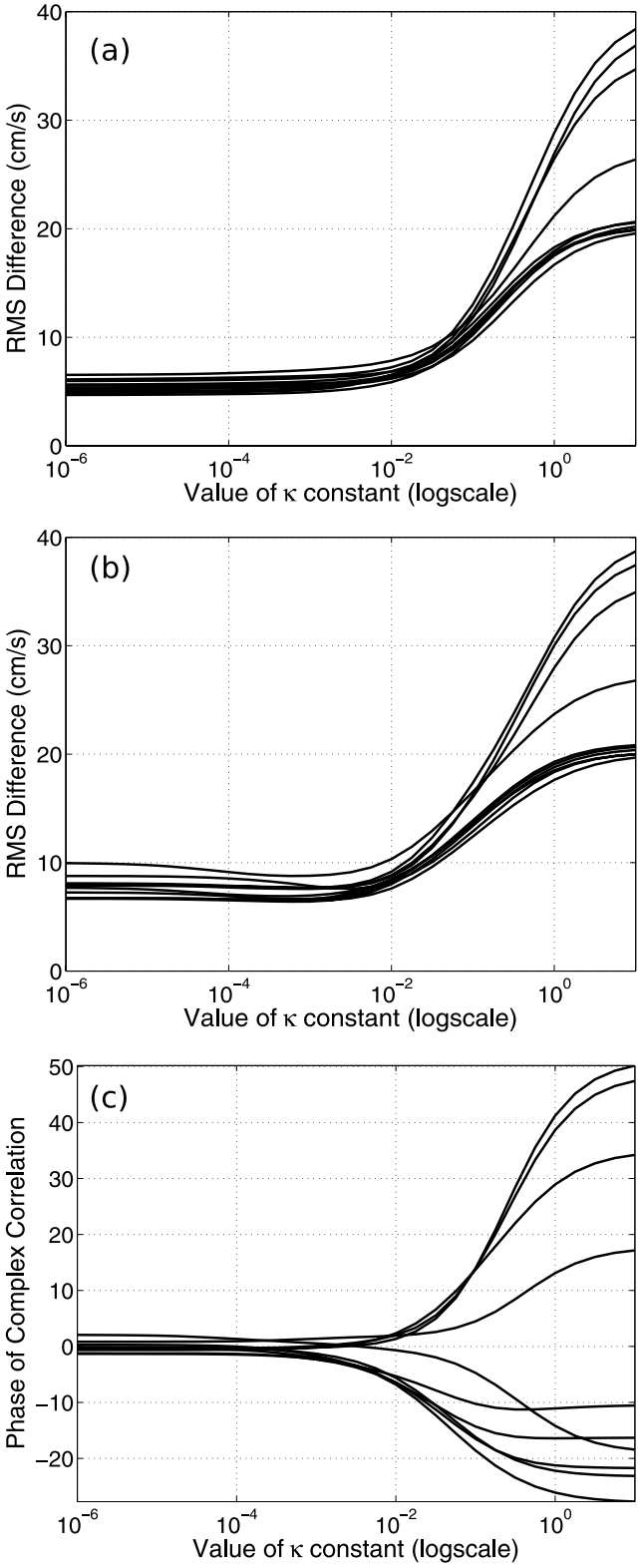

Figure 7. Difference between total current measurements and fitted current vectors as a function of the coefficient of the homogenization smoothing term, κ, for the 10 hours of data with the worse spatial coverage for the Bodega Bay array (similar results were obtained for periods with good spatial coverage). (a, b) RMS differences. (c) Phase (in degrees) of complex correlations, a measure of the angle difference between velocity vectors. In Figure 7a, modes on the small domain were fit to total current vectors, while in Figures 7b and 7c, modes on the small domain were fit to radial currents, the result of which was then compared to the total currents data. In both cases, the minimum spatial scale of the modes is 5 km. The x axis on all plots is on a $\log_{10}$ scale. Note that RMS differences and phases change little for κ less than approximately 10^{-2}. Also note that RMS differences approach the RMS speed of the total current measurements themselves as the value of κ becomes large (right-hand side of Figures 7a and 7b) because fitted currents become small.

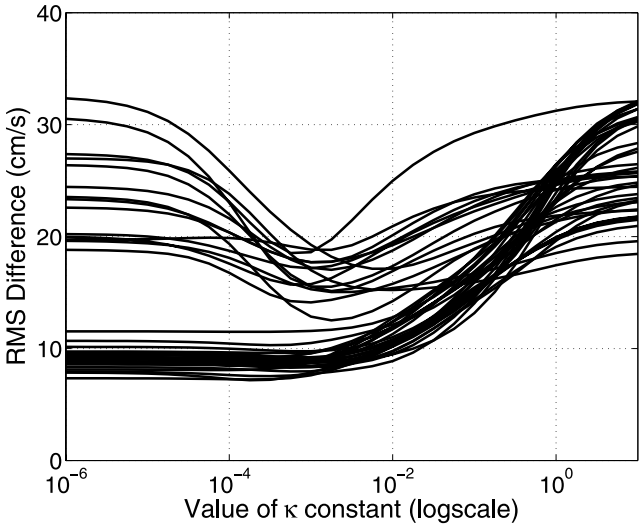

Figure 8. RMS difference between total current measurements and fitted currents in Monterey Bay as a function of the coefficient of the homogenization smoothing term, κ. The curves are for 42 hours of data for which one of the four HF radars in Monterey was not functioning. Those curves with high RMS differences at small values of κ are for time periods with extremely large gaps in coverage by radial current measurements due to the failure of the Santa Cruz radar.

current velocity and spatial structure throughout the domain (Figure 4d).

[58] The optimal value for κ can be determined by comparing the fitted current field with the original total currents measurements. Fits based on both total currents and radial currents show that the maximum value of κ that does not diminish the fit to the original data is of order 10^{-4}–10^{-2} (Figure 7). This maximum value of κ is robust with respect to the size of the domain and the location of the domain (e.g., results are similar for data from Monterey Bay; Figure 8).

[59] Note that RMS differences between fitted currents and total current measurements are in general lower when this fit is based on total current measurements than when it is based on radial currents (Figure 7a versus 7b). The goal of the fit to radial current data is to minimize the difference with respect to that data, not the total current measurements. As a result, RMS differences with respect to total current measurements are in general higher. This does not indicate, however, that the fitted current field is a worse representation of the actual flow field. The OMA fits to radial data take into account information on multiple spatial scales when determining the current at a location, as opposed to just those closest to the point, as in the standard method of generating total currents from radial data. Therefore the OMA fits may represent a better estimate of the actual flow field.

[60] RMS differences between OMA fits to radial data and normal total current measurements can decrease as κ is increased from very small values. This is particularly evident in fits with very large data gaps in Monterey Bay due to the failure of the Santa Cruz radar (Figure 8). The reason for this is that the magnitude of large, unphysical current vectors decreases as κ increases. When there are very large gaps, this will affect fitted currents even in regions where radial current data exists, thereby reducing the overall RMS difference. This is further confirmation that a value of κ in the range 10^{-4}–10^{-2} is sufficient to make the fit nonsingular without overly damping the fitted current field. However, fits with such large data gaps are probably not recommendable under most circumstances.

4.3. Uncertainty Estimate

[61] Estimated errors for the fitted current fields based on error propagation depends on the assumed error structure of the data measurements, the minimum spatial scale of the modes and the value of κ. Uncertainties are highest in areas with a low density of data measurements, exceeding 1 m/s inside large data gaps (Figure 9). Errors were also consistently large along the line of sight between radar stations. Particularly large errors are found in the northeast portion of the Bodega domain (Figure 10a), in apparent contradiction to the high density of radial data available in this area (Figure 3b). This dense data originates, however, mostly from a single radar station. This indicates that instabilities in the fit and, consequently, large propagated errors in the fitted current field are due, not only to the absence of data, but also to its inability to resolve both components of the flow field.

[62] When a uniform measurement error was assumed for all data, error estimates were based solely on the density of data and the spatial geometry of the data. In this case, propagated errors tended to be more homogeneous spatially compared to results using the measured variance in radial current measurements (i.e., compare Figures 9a and 9b). Furthermore, the error field produced using the measured radial current variances had higher values in some parts of the domain, particularly the southwestern corner (Figure 9b), that correspond to areas of lower data quality [*Kaplan et al.*, 2005].

[63] Error estimates differed substantially depending on the number of modes used in the fit (and, therefore, the minimum spatial scale of the modes). Errors are lower and more homogeneous when the minimum spatial scale of the modes is 10 km, as opposed to 5 km (compare Figures 9a and 9b with Figures 9c and 9d). These differences correspond to the fact that less of the overall spatial variance is represented in the fit with fewer modes, and, therefore, the certainty in the mode coefficients is higher if fewer modes are used. However, the certainty in the difference between the fitted current at a location and the true current at that location increases due to this unaccounted small-scale spatial variability.

[64] Increasing the value of κ reduced the propagated error values, though reductions were minimal in areas with data for values of κ less than about 10^{-4}. Changes in error values were considerable, even for small values of κ, in parts of the domain without data. For example, for the time period and configuration shown in Figure 9b, error values along the northern edge of the domain reached 10 m/s when $\kappa = 0$ (not shown), considerably larger than values obtained for $\kappa = 10^{-4}$. These changes correspond to the large

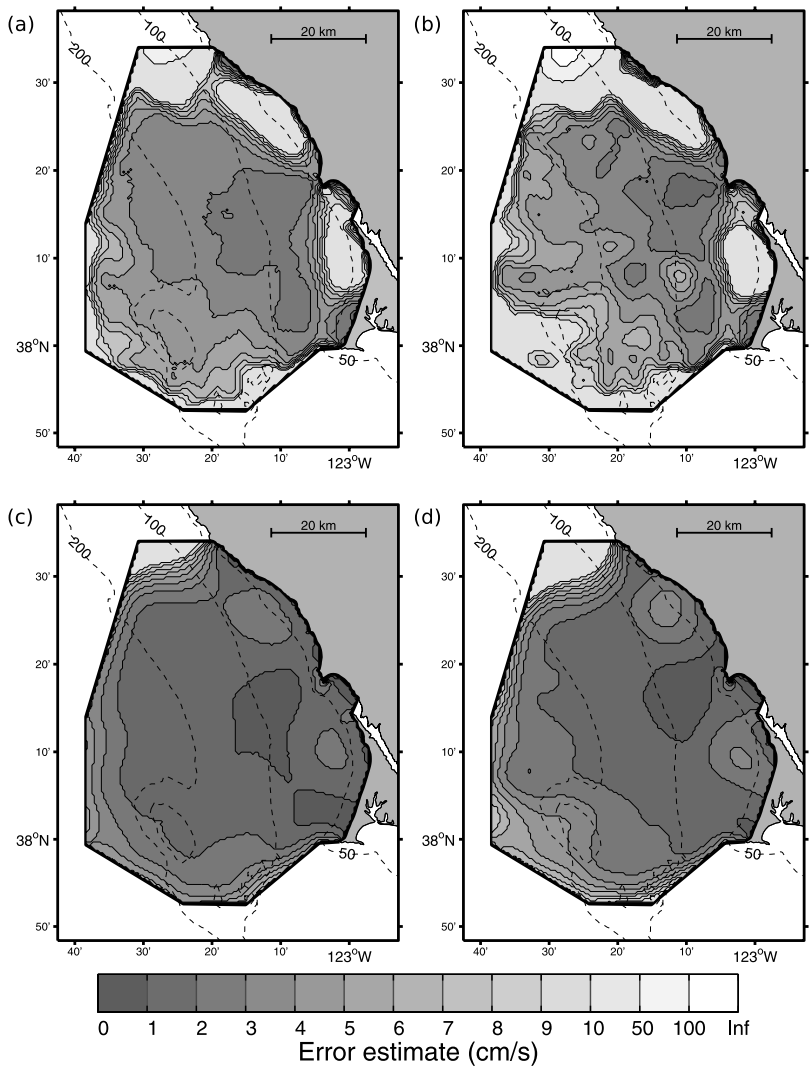

Figure 9. Error propagation results for the fit on the large domain with $\kappa = 10^{-4}$ for radial current measurements from 30 July 2003 1500 PST (as in Figure 4). Errors shown are the square root of the sum of the *u* and *v* variances and are given in cm/s. In Figures 9a and 9b, modes had a minimum spatial scale of 5 km, while in Figures 9c and 9d, modes had a minimum spatial scale of 10 km. In Figures 9a and 9c, errors are based on the assumption that all radial data has a uniform variance of 7.5 cm/s and that covariance among radial measurements is zero. In Figures 9b and 9d, errors are the result of propagating to the fitted current field the measured radial current variances (from repeated radial measurements during a single hour). As in Figures 9a and 9c, covariance among measurements is assumed zero in Figures 9b and 9d. Note that contour levels are not uniformly spaced above 10 cm/s.

reduction in fitted currents in this area with nonzero κ values (Figure 4).

[65] The error structure obtained from error propagation corresponded well with those obtained by bootstrapping the fit to the data (Figure 11) both in value and in spatial structure. The spatial structure of the bootstrapped error field appears visually to correspond most closely with the propagated error field when measured radial variances were used. This is somewhat surprising as one would expect it to correspond most closely with an assumption of uniform measurement error as no particular distribution was used in determining which measurements were selected when the data was resampled.

4.4. Effect of Weighting Radial Current Measurements

[66] The effect of weighting measurements in the fit to the modes by data density (see section 3.3) was measured by computing RMS differences between fits with and without the weights for 100 time steps with high data availability (so as to remove the effect of large data gaps; Figure 10b). RMS differences tended to be low compared to propagated error values (Figure 10a). Nonetheless, differences had a consistent spatial pattern with largest changes concentrated in areas with consistently low data availability, along the line of sight between radars and along the western edge of the domain. Surprisingly, weights did not dramatically affect fitted currents in areas of high data density, such as near HF radar sites.

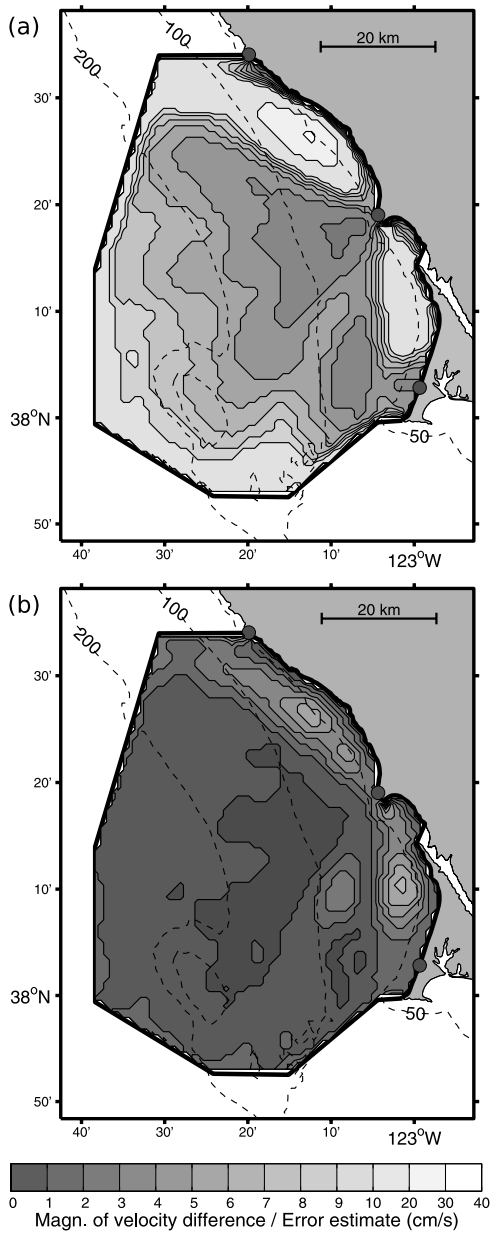

Figure 10. (a) Square root of the time-averaged total variance (sum of the u and v variances) based on error propagation and (b) RMS magnitude of the velocity difference between fits to radial current measurements with and without weightings of radial vectors based on data density. Values are in cm/s and results shown are from modal fit on the large domain with 5 km spatial resolution. RMS calculations are over the 100 hourly current maps with the best radial coverage. Current velocity error estimates are based on the measured radial current variances.

4.5. Divergence and Vorticity

[67] Divergence and vorticity maps were computed from the fit to the modes over the entire time series and then averaged over upwelling and relaxation periods (see theory in section 2.2). Though the resulting divergence maps are noisy and quite complex spatially (Figure 12), they generally agree with similar divergence maps derived from spatial derivatives of HF radar total current measurements given by *Kaplan and Largier* [2006]. Divergence values are generally positive (upwelling favorable) over most of the domain during upwelling periods (Figure 12a), whereas they are more spatially complex and mixed between positive and negative values during relaxation periods (Figure 12b). Vorticity maps (Figure 13) tended to have a more consistent spatial pattern with considerable positive vorticity over most of the inner shelf and midshelf, and moderate to small negative vorticities over the outer shelf. This pattern agrees with the strong cross-shore gradient in the alongshore flow field noted by *Kaplan et al.* [2005] and *Kaplan and Largier* [2006].

[68] An important goal of this paper is to assess the robustness of the OMA decomposition to calculate divergence and vorticity patterns. There are features in the modal divergence and vorticity maps that did not appear in the direct computation of these maps from raw data [*Kaplan and Largier*, 2006]. For example, average divergence and vorticity during relaxation periods have large magnitudes and fluctuations in the nearshore regions north and south of the BML radar station when modes with a 5 km spatial scale are used. With the exception of the area of negative vorticity near the end of Pt. Reyes Peninsula, which has been associated with poleward flow around the point during relaxation periods [*Kaplan and Largier*, 2006], none of these features are related to known physical processes in the region. These features occur in areas of low data coverage, suggesting that they are artifacts of instabilities in the fit to the data.

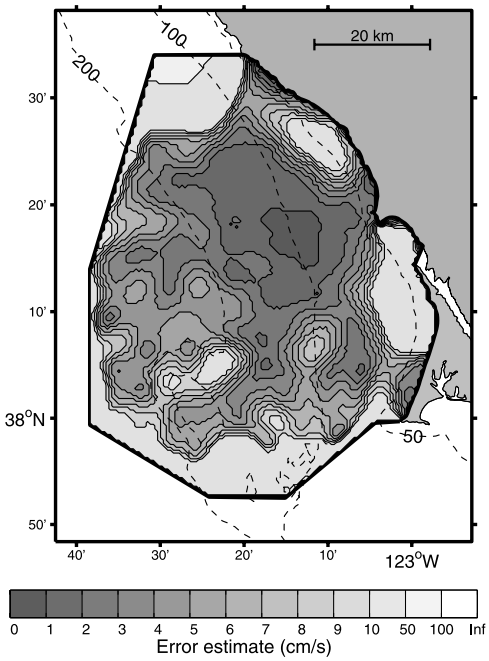

Figure 11. Uncertainties based on bootstrap of fit to modes for the same time period as shown in Figures 4 and 9 using a value of 10^{-4} for the homogeneous smoothing term, κ. Values shown are the square root of the sum of the u and v variances and are given in cm/s. Note that contour levels are not uniformly spaced above 10 cm/s.

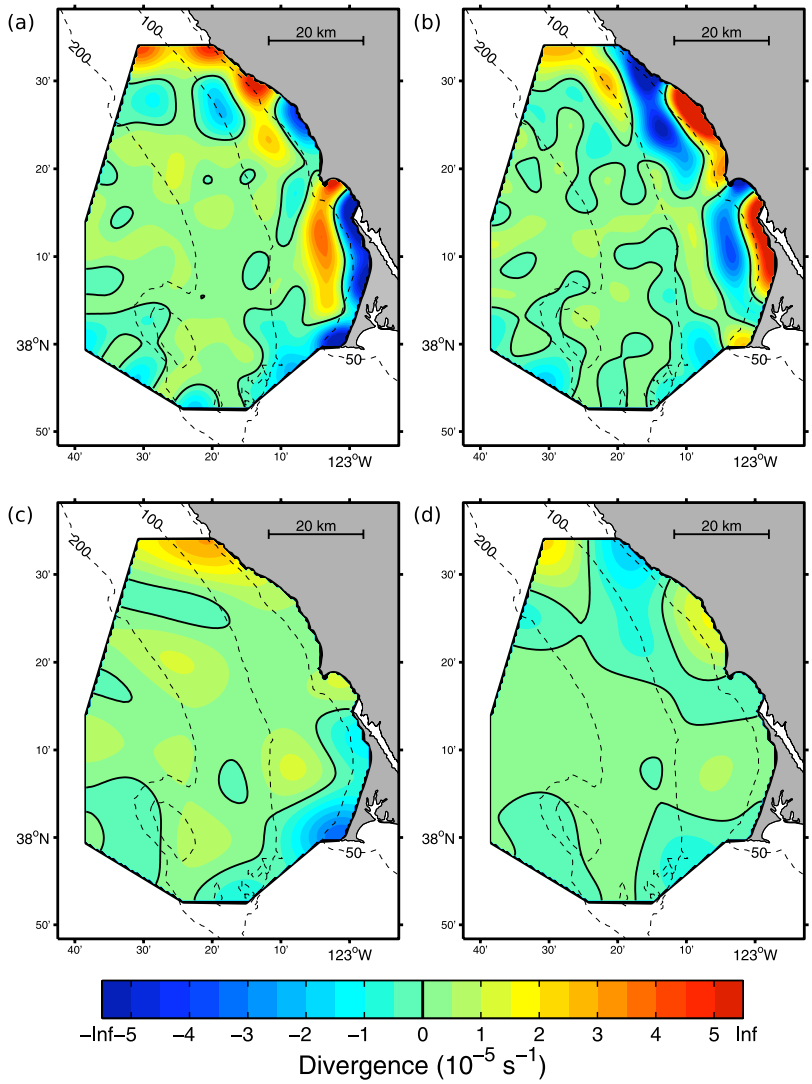

Figure 12. Average patterns of divergence for (a, c) upwelling and (b, d) relaxation periods, as defined by the alongshore wind stress. Figures 12 a and 12b show divergence results for the fit using modes with a minimum spatial scale of 5 km, while Figures 12c and 12d are for a spatial scale of 10 km. The thick, black contour indicates zero divergence.

[69] Time-averaged propagated uncertainties and temporal standard deviations for divergence (not shown) and vorticity (Figure 14) indicate that these features are indeed subject to large uncertainties. Typical error values are of the same order as the average divergences and vorticities throughout the domain. This is to some degree an unavoidable consequence of calculating small differences between noisy measurements (like divergence and vorticity). Note, however, that these errors represent the level of confidence that the divergence or vorticity map in an individual hour will resemble the mean pattern. If one is interested in the confidence in the mean (i.e., the standard error as opposed to the standard deviation), then these errors must be reduced by the square root of the number of degrees of freedom. Assuming that roughly 60 days of measurements went into each divergence/vorticity map for upwelling/relaxation periods and a temporal autocorrelation timescale or approximately 2 days [*Kaplan et al.*, 2005], then the standard error is approximately a factor of 5.5 smaller than those in Figure 14. Though these errors are still considerable, there is much more certainty in the mean than in an individual hourly pattern of divergence.

[70] Uncertainty values were largest in the nearshore areas between the radars and along the northern edge of the domain, where data quality and coverage have previously been identified as poor. Furthermore, if the value of the homogeneous smoothing term, κ, is set to zero, then error estimates in these areas of marginal data coverage increases substantially (not shown), indicating that the true uncertainty in divergence and vorticity is quite high there. Standard deviations (Figures 14c and 14d) are somewhat more widely distributed than propagated uncertainties (Figures 14a and 14b), suggesting that there are time-varying deterministic processes that are not captured by the long-term average divergence and vorticity patterns. Uncertainties in the divergence and vorticity patterns from the fit to modes with a 10 km spatial scale are considerably smaller (not shown), particularly when compared to the

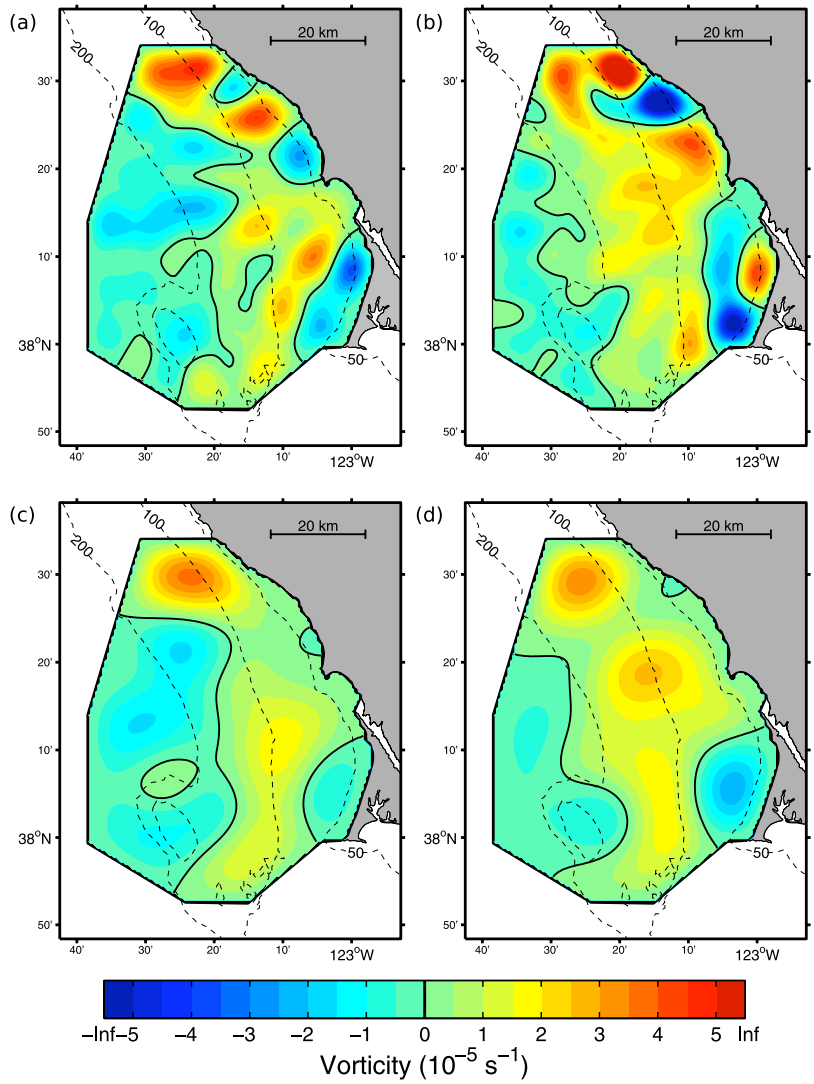

Figure 13. Average patterns of vorticity for (a, c) upwelling and (b, d) relaxation periods, as defined by the alongshore wind stress. Figures 13a and 13b show vorticity results for the fit using modes with a minimum spatial scale of 5 km, while Figures 13c and 13d are for a spatial scale of 10 km. The thick, black contour indicates zero vorticity.

average patterns, suggesting that divergence and vorticity patterns at this spatial scale are more trustworthy. Note that uncertainties in the vorticity are constrained to be zero along the entire domain edge. This is an artifact of the fit directly related to the constraint that vorticity be zero along the domain edge (see section 2.2) and does not represent the true uncertainty.

5. Discussion

[71] In this paper, we presented recent advances in open-boundary modal analysis (OMA) and highlighted unresolved issues. We focused on its application to HF radar data sets and on identifying the advantages and disadvantages of the technique. We have shown that modal current decomposition is a flexible technique for interpolating and spatially aggregating two-dimensional current measurements that is capable of addressing some of the limitations of these data. Particularly valuable are its incorporation of the coastal boundary condition, the ability to naturally control the minimum spatial scale of the fitted current field, the direct calculation of divergence and vorticity fields, and the transparent estimation of uncertainties in the final current fields. The technique is two-dimensional, and, therefore, has the advantage of not requiring any knowledge of the full three-dimensional circulation pattern. However, this has the disadvantage of not allowing the incorporation of additional constraints on the circulation pattern from fully three-dimensional circulation data, and extensions that incorporate such three-dimensional information may be desirable in the future.

[72] We have also shown that modal current decomposition can be applied directly to HF radar radial current measurements. This suggests that this technique provides an alternative to the usual approach for generating total current velocity fields from HF radar data [e.g., *Lipa*, 2003]. After fitting current measurements to the modes, maps of uncertainty measurements (e.g., Figure 9) can be used to

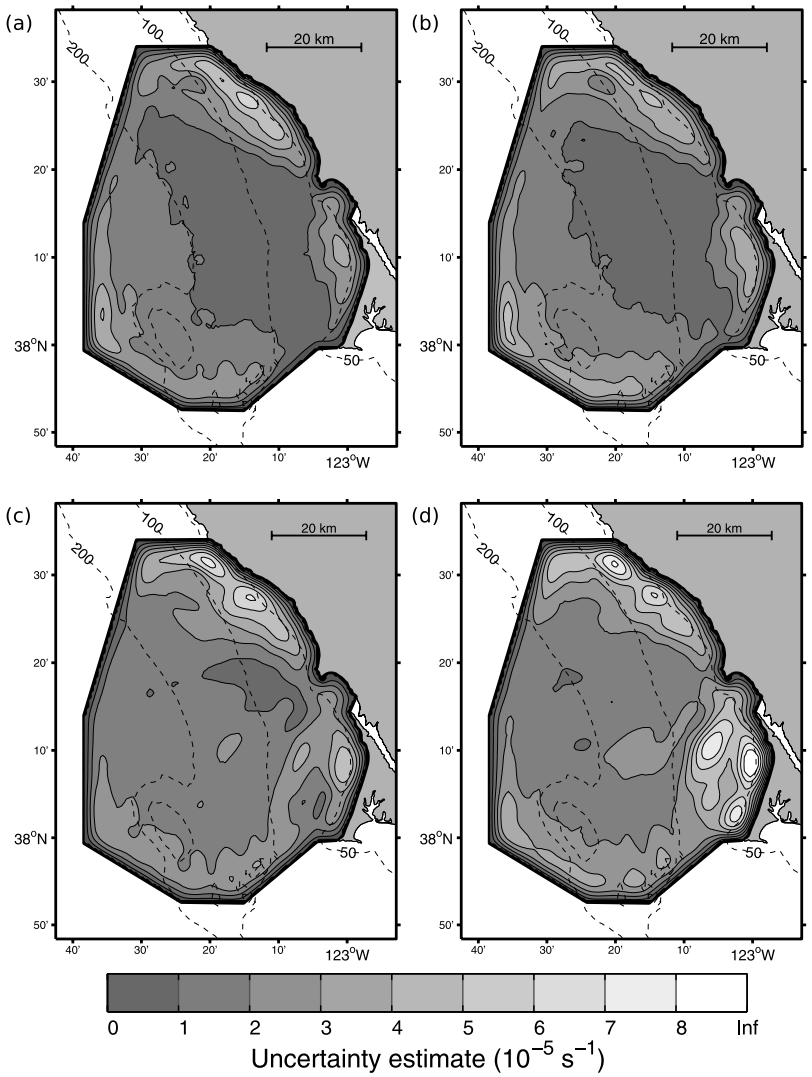

Figure 14. (a, b) Square root of the time-averaged uncertainties (from error propagation) in vorticity and (c, d) temporal standard deviation of vorticity estimates. Figures 14a and 14c are for upwelling periods, while Figures 14b and 14d are for relaxation periods. Results are for fits using modes with a minimum spatial scale of 5 km.

eliminate those fitted current vectors that do not satisfy an error and/or signal-to-noise-ratio bound. This will produce a discontinuous current field just as the normal technique of combining radial current measurements into total currents does. Though it is also possible to propagate uncertainties forward with the standard method [*Lipa*, 2003], this method cannot incorporate the complex boundary condition along the shoreline. Furthermore, modal current decomposition produces uncertainty measurements that are referenced by spatial scale (i.e., there is an uncertainty for each mode coefficient). This information can potentially be used to more accurately assess uncertainties in current measurements with different levels of spatial aggregation and precisely identify the spatial limitations of HF radar data sets. Uncertainty maps like that in Figure 10a clearly identify areas where additional HF radar coverage would be beneficial and may aid in radar site selection. Finally, while the initial calculation of the modes on large meshes might take several hours, once the modes have been generated, fitting data to those modes can be quicker than the normal method of generating total current vectors and allows one to only keep track of a number of variables that is commensurate with the level of spatial aggregation desired (i.e., the mode coefficients).

[73] While the basic technique is robust, we have identified several aspects of the technique that need to be considered carefully. Data gaps and/or data from a single radar station can produce fitted current fields that have large uncertainties due to instabilities in the least squares fit to these data. While the addition of the homogeneous term to the fit does dramatically reduce large, unphysical fitted current vectors with little reduction in the comparison between the fitted currents vectors and current vectors calculated via the normal non-OMA method for small κ values, this must not be confused with improving the quality of the fitted current vectors. For example, if the value of κ is chosen to be too large, the currents and uncertainties over the entire domain will be small. This is clearly erroneous

and indicates the peril of using the homogeneous smoothing term without careful consideration.

[74] The propagated uncertainties themselves must be interpreted with care. This is clear from the considerable decrease in uncertainties when the minimum mode spatial scale is increased (Figure 9). This decrease is due to the fact that increasing the minimum mode spatial scale decreases the amount of spatial variability in the fitted current field, as well as removes the associated uncertainty in the current field at those spatial scales. Therefore propagated errors must not be viewed as the true uncertainty in the fitted current field, but rather the uncertainty up to a specific spatial scale. There is additional uncertainty corresponding to sub-mode-scale spatial variability in the current field that is not captured in the propagated error field. This same problem affects the standard method of generating total current measurements (in that case sub-grid-scale variability), which has been assessed via comparisons with other in situ current measurements (e.g., moored ADCP data [*Kaplan et al.*, 2005; *Ullman et al.*, 2006]). The same procedure could be used in this case. One can also compare fitted current fields at two different spatial scales, one that is very small and the other that is more appropriate for the particular problem of interest, to assess part of this remaining uncertainty (similar to Figure 7).

[75] It is also important to understand the relationship between the propagated errors discussed here and the more familiar geometric dilution of precision (GDOP) error estimate of total current measurements. As used in the HF radar community, GDOP is the error estimate that would result from error propagation in the normal method of generating total vector currents (by inverting nearby radial measurements to get a velocity estimate at a location) if one assumes that all radial measurements have a uniform uncertainty of 1 and there is no covariance between the radial errors. As this estimate does not include actual measurements of radial uncertainty, it is purely based on the angles of the radial measurements (explaining the word ''geometric'' in GDOP). The error estimate based on error propagation presented by *Lipa* [2003] is a natural extension of GDOP to a fully nonuniform error covariance matrix. It includes both ''geometric'' effects and effects due to spatial variability in data quality. Similarly, the propagated errors presented in section 3.4 include effects due to the spatial geometry of the data and the measured uncertainty in each radial measurement, as evidenced by the large errors in areas with data from only one radar or poor data quality (Figure 10a). Therefore the errors presented here are analogous to and contain the same types of information as the estimates of uncertainty produced by GDOP and its more general extension [*Lipa*, 2003]. As such, they are a useful assessment of spatial patterns of uncertainty that should be integrated into the evaluation and study of HF radar current measurements.

[76] Though spatial patterns of divergence were consistent with prior results [e.g., *Kaplan and Largier*, 2006], they were also subject to considerable errors. This is not surprising as derivatives of noisy measurements are inherently subject to relatively large errors. The advantage of using modal current decomposition to calculate divergence and vorticity fields is that it provides a straightforward way to calculate these fields with a fixed level of spatial smoothing and to estimate their uncertainties.

[77] This paper highlights one important limitation to our ability to assess the uncertainties in HF radar current measurements and derived products: the lack of an understanding of the structure of the radial uncertainty covariance matrix. Without an idea of how uncertainty in radial and total current measurements are correlated over space, it is impossible to accurately estimate error. The assumption of a diagonal covariance matrix (i.e., zero covariance among measurement errors) will inevitably overestimate the true number of independent measurements and lead to unjustifiably low current velocity error estimates. The use of weights in the fit to the modes based on the density of radial data does not appear to adequately address problems of high data density and data covariance, though weighting may play a role in the final solution to these problems. The study of radial data uncertainties and error covariance remains an important direction of future research.

[78] Despite the need for attention in applying modal current decomposition to HF radar data, we have shown that the method has a number of important advantages. The combination of modal fitted current fields with propagated errors provides a robust approach to calculating and analyzing surface current measurements.

[79] **Acknowledgments.** We are grateful to Michael Cook (NPS), Daniel Atwater (UCSC), Chad Coulliette (Griffon Laboratories), Ed Dever (OSU), Bruce Lipphardt (University of Delaware), Christopher A. Edwards (UCSC), and John L. Largier (BML, UCD) for many useful conversations and e-mails. We thank Hezi Gildor (Weizmann Institute of Science) and Don Barrick (CODAR Ocean Systems) for sharing their thoughts on using radial data instead of totals. D. M. K thanks Dennis Kirwan (University of Delaware) for a useful email confirming that vorticity vanishes at the coastline. The work of D. M. K. was supported by NSF CoOP Project grant OCE-9907884 and the Coastal Ocean Currents Monitoring Program (COCMP) funded by the California State Coastal Conservancy. The work of F. L. was partially supported by ONR grants N00014-02-1-0826 and N0014-04-1-0534.

References

Amit, Y. (1994), A non-linear variational problem for image matching, *SIAM J. Sci. Comput.*, *15*, 207–224.

Bjorkstedt, E., and J. Roughgarden (1997), Larval transport and coastal upwelling: An application of HF radar in ecological research, *Oceanography*, *10*, 64–67.

Brandt, S. (1983), *Statistical and Computational Methods in Data Analysis*, 414 pp., Elsevier, New York.

Brunnet, G., H. Hagen, and G. Sapiro (1997), Geodesic active contours, *Int. J. Comput. Vision*, *22*, 61–79.

Chapman, R. D., L. K. Shay, H. C. Graber, J. B. Edson, A. Karachintsev, C. L. Trump, and D. B. Ross (1997), On the accuracy of HF radar surface current measurements: Intercomparisons with ship-based sensors, *J. Geophys. Res.*, *102*, 18,737–18,748.

Chu, P. C., L. M. Ivanov, T. P. Korzhova, T. M. Margolina, and O. V. Melnichenko (2003), Analysis of sparse and noisy ocean current data using flow decomposition, Part I: Theory, *J. Atmos. Oceanic Technol.*, *20*, 478–491.

Coulliette, C., F. Lekien, J. D. Padan, G. Haller, and J. E. Marsden (2007), Optimal pollution mitigation in Monterey Bay based on coastal radar data and nonlinear dynamics, *Environ. Sci. Technol.*, *41*(18), 6562–6572.

Eiseman, P. R., and A. P. Stone (1973), Hodge decomposition theorem, *Not. Am. Math. Soc.*, *20*(20), A169.

Hodgins, D. O. (1994), Remote-sensing of ocean surface currents with the Seasonde HF radar, *Spill Sci. Technol. Bull.*, *1*, 109–129.

Kaplan, D. M., and J. L. Largier (2006), HF radar-derived origin and destination of surface waters off Bodega Bay, California, *Deep Sea Res., Part II*, *53*, 2906–2930.

Kaplan, D. M., J. L. Largier, and L. W. Botsford (2005), HF radar observations of surface circulation off Bodega Bay (northern California, USA), *J. Geophys. Res.*, *110*, C10020, doi:10.1029/2005JC002959.

Lekien, F., C. Coulliette, R. Bank, and J. Marsden (2004), Open-boundary modal analysis: Interpolation, extrapolation, and filtering, *J. Geophys. Res.*, *109*, C12004, doi:10.1029/2004JC002323.

Lekien, F., C. Coulliette, A. J. Mariano, E. H. Ryan, L. K. Shay, G. Haller, and J. E. Marsden (2005), Pollution release tied to invariant manifolds: A case study for the coast of Florida, *Physica D*, *210*, 1–20.

Lipa, B. J. (2003), Uncertainties in SeaSonde Current Velocities, paper presented at IEE/OES Seventh Working Conference on Current Measurement Technology, Inst. of Electr. and Electron. Eng., San Diego, Calif.

Lipphardt, B., Jr., A. Kirwan Jr., C. Grosch, J. Lewis, and J. Paduan (2000), Blending HF radar and model velocities in Monterey Bay through normal mode analysis, *J. Geophys. Res.*, *105*, 3425–3450.

Lynch, P. (1989), Partitioning the wind in a limited domain, *Mon. Weather Rev.*, *117*, 1492–1500.

Olascoaga, M. J., I. I. Rypina, M. G. Brown, F. J. Beron-Vera, H. Kocak, L. E. Brand, G. R. Halliwell, and L. K. Shay (2006), Persistent transport barrier on the West Florida shelf, *Geophys. Res. Lett.*, *33*, L22603, doi:10.1029/2006GL027800.

Paduan, J. D., and L. Rosenfeld (1996), Remotely sensed surface currents in Monterey Bay from shore-based HF radar (Coastal Ocean Dynamics Application Radar), *J. Geophys. Res.*, *101*, 20,669–20,686.

Pottmann, H., and S. Leopoldseder (2003), A concept for parametric surface fitting which avoids the parametrization problem, *Comput. Aided Geometric Design*, *20*, 343–362.

Shadden, S. C., F. Lekien, J. D. Paduan, F. P. Chavez, and J. E. Marsden (2007), The correlation between surface drifters and coherent structures based on high-frequency radar data in Monterey Bay, *Deep Sea Res., Part II*, in press.

Ullman, D. S., J. O'Donnell, J. Kohut, T. Fake, and A. Allen (2006), Trajectory prediction using HF radar surface currents: Monte Carlo simulations of prediction uncertainties, *J. Geophys. Res.*, *111*, C12005, doi:10.1029/2006JC003715.

D. M. Kaplan, Centre de Recherche Halieutique, Institut de Recherche pour le Developpement, Avenue Jean Monnet, BP171, F-34203 Sete, France. (david.kaplan@ird.fr)

F. Lekien, École Polytechnique, Université Libre de Bruxelles, CP 165/11, 50 F. D. Roosevelt Avenue, 8-1050 Brussels, Belgium. (lekien@ulb.ac.be)